PHYSICAL REVIEW B **94**, 104423 (2016)

Strong magnetoelastic coupling at the transition from harmonic to anharmonic order in $NaFe(WO_4)_2$ with $3d^5$ configuration

S. Holbein,[1,2] M. Ackermann,[3,*] L. Chapon,[2] P. Steffens,[2] A. Gukasov,[4] A. Sazonov,[4,†] O. Breunig,[1] Y. Sanders,[1]
P. Becker,[3] L. Bohatý,[3] T. Lorenz,[1] and M. Braden[1,‡]
[1]*II. Physikalisches Institut, Universität zu Köln, Zülpicher Strasse 77, D-50937 Köln, Germany*
[2]*Institut Laue-Langevin, 71 avenue des Martyrs, F-38042 Grenoble Cedex 9, France*
[3]*Abteilung Kristallographie, Institut für Geologie und Mineralogie, Universität zu Köln, Greinstrasse 6, 50939 Köln, Germany*
[4]*Laboratoire Léon Brillouin, CEA/CNRS, F-91191 Gif-sur-Yvette, France*

(Received 7 July 2016; revised manuscript received 30 August 2016; published 21 September 2016)

The crystal structure of the double tungstate $NaFe(WO_4)_2$ arises from that of the spin-driven multiferroic $MnWO_4$ by inserting nonmagnetic Na layers. $NaFe(WO_4)_2$ exhibits a three-dimensional incommensurate spin-spiral structure at low temperature and zero magnetic field, which, however, competes with commensurate order induced by magnetic field. The incommensurate zero-field phase corresponds to the condensation of a single irreducible representation but it does not imply ferroelectric polarization because spirals with opposite chirality coexist. Sizable anharmonic modulations emerge in this incommensurate structure, which are accompanied by large magnetoelastic anomalies, while the onset of the harmonic order is invisible in the thermal-expansion coefficient. In magnetic fields applied along the monoclinic axis, we observe a first-order transition to a commensurate structure that again is accompanied by large magnetoelastic effects. The large magnetoelastic coupling, a reduction of the b lattice parameter, is thus associated only with the commensurate order. Upon releasing the field at low temperature, the magnetic order transforms to another commensurate structure that considerably differs from the incommensurate low-temperature phase emerging upon zero-field cooling. The latter phase, which exhibits a reduced ordered moment, seems to be metastable.

DOI: 10.1103/PhysRevB.94.104423

I. INTRODUCTION

In so-called type-II multiferroics a complex magnetic order directly drives spontaneous ferroelectric polarization opening the path for possible applications in data storage or calculation technologies [1]. In most of the newly discovered multiferroics, in particular in the prototype multiferroic materials $R\mathrm{MnO}_3$ with R for example Tb or Dy [2], the coupled ferroelectric polarization is explained by the inverse Dzyaloshinskii-Moriya mechanism [3–5]. While in typical magnetic systems antisymmetric coupling arises from a low crystal symmetry and induces spin canting, an intrinsically noncollinear magnetic structure can drive a structural distortion and thereby enhance or even create antisymmetric coupling. However, only if this structural distortion also develops a macroscopic ferroelectric polarization is the system multiferroic. The antisymmetric coupling is induced by spin-orbit coupling and therefore is much smaller than the dominant symmetric exchange interaction. In consequence, the ferroelectric polarization values induced by the inverse Dzyaloshinskii-Moriya mechanism are typically small [1], two or more orders of magnitude smaller than in a normal ferroelectric. Modifying the symmetric and isotropic exchange seems more promising to obtain multiferroics with large ferroelectric polarization, and it was proposed [6] and experimentally confirmed [7] that orthorhombic $R\mathrm{MnO}_3$ with smaller R exhibit such a large multiferroic polarization based on exchange striction. For smaller R the magnetic structure changes from the incommensurate cycloid observed for Tb or Dy to a commensurate up-up-down-down structure (called "E type"), in which the scalar product of neighboring moments entering the symmetric exchange even changes sign. This exchange-striction-based magnetoelectric coupling [6] not only explains the static coupling in the multiferroic phase of the E-type ordered $R\mathrm{MnO}_3$, but it also constitutes the dominant dynamic magnetoelectric coupling resulting in the strongest electromagnon modes [8,9] in the $R\mathrm{MnO}_3$ with larger R that exhibit the incommensurate cycloidal order. The distinct multiferroic phases in $R\mathrm{MnO}_3$ thus arise from the competition between incommensurate cycloid and commensurate up-up-down-down orders, and this competition is controlled through the structural distortions following the R ionic radius. Here, we investigate $NaFe(WO_4)_2$, which also exhibits a competition between incommensurate cycloid and up-up-down-down phases, and which, therefore, may help in understanding the complex magnetoelastic coupling in such phase diagrams. Also in $NaFe(WO_4)_2$ we find rather strong magnetoelastic coupling, however without any ferroelectric polarization so that none of the phases of $NaFe(WO_4)_2$ is multiferroic.

The discovery of a spin-driven multiferroic phase in $MnWO_4$ in 2006 [10–12] motivated the search for multiferroicity in other materials of the tungstate family [13]. The magnetic moments in $MnWO_4$ develop a spin spiral at low temperature which is the driving force of the ferroelectric polarization, explained by the inverse Dzyaloshinskii-Moriya mechanism [2–5]. The metal ion M^{2+} in $M\mathrm{WO}_4$ can be substituted by a magnetic ion with the same valency or by a combination of mono- and trivalent ions. The resulting compounds often

---

[*] Present address: TRUMPF Laser GmbH.

[†] Present address: Institute of Crystallography, RWTH Aachen University, and Jülich Centre for Neutron Science (JCNS) at Heinz Maier-Leibnitz Zentrum, 85747 Garching, Germany.

[‡] braden@ph2.uni-koeln.de

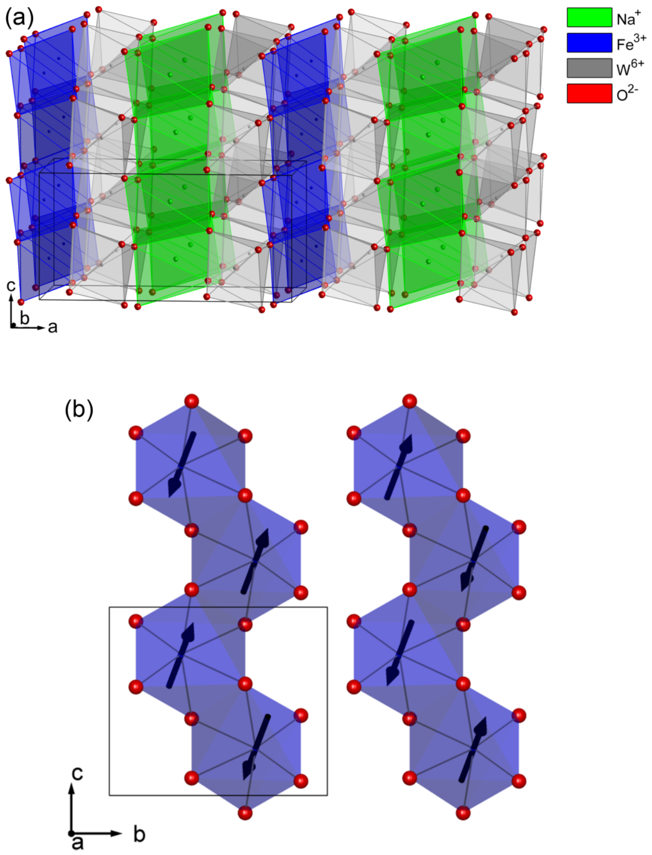

FIG. 1. (a) Crystal structure of $NaFe(WO_4)_2$. Tungsten, iron, and sodium ions are surrounded by oxygen octahedra. These octahedra form edge-sharing chains along $\vec{c}$ and order in planes perpendicular to $\vec{a}$. (b) Zigzag chains of iron octahedra propagate along $\vec{c}$. The arrows show the magnetic up-up-down-down structure with propagation vector $\vec{k}_{\rm com} = (0.5,0.5,0.5)$ [16]. The black box indicates the crystallographic unit cell.

develop a simple collinear antiferromagnetic structure, which is the case for $FeWO_4$ [14], $CoWO_4$, $NiWO_4$, $CuWO_4$ [15], and $NaCr(WO_4)_2$ [16]. No electric polarization was observed in these compounds [13].

The crystal structure of the double tungstate $NaFe(WO_4)_2$ can be described in the monoclinic space group $P2/c$ with lattice parameters $a = 9.88$ Å, $b = 5.72$ Å, $c = 4.94$ Å, and a monoclinic angle of $\beta = 90.33^\circ$ [17]. Na^+ and Fe^{3+} ions are surrounded by edge-sharing $[O_6]$ octahedra. These octahedra form zigzag chains along $\vec{c}$ and align in planes parallel to the *bc* plane. The crystal structure is shown in Fig. 1(a). Layers containing $[NaO_6]$ and $[FeO_6]$ octahedra, respectively, are separated by layers that contain $[WO_6]$ octahedra only. Due to the insertion of the Na planes the unit cell of $NaFe(WO_4)_2$ is doubled along $\vec{a}$, with respect to the natural wolframites $MnWO_4$ and $FeWO_4$, which otherwise crystallize in the same space group [14,15]. Therefore, the magnetic interaction between Fe^{3+} is considerably weakened along $\vec{a}$ resulting in a lower Néel temperature.

Similarly to the case of $MnWO_4$, the magnetic Fe^{3+} ions in $NaFe(WO_4)_2$ form zigzag chains along the *c* axis [see Fig. 1(b)]. In spite of the long distance between the Fe^{3+} ions in adjacent layers, $NaFe(WO_4)_2$ develops a three-dimensional magnetic structure at temperatures below 4 K. The analysis of neutron powder diffraction yielded a collinear antiferromagnetic structure with magnetic moments aligned parallel to the *a* axis [16]. The magnetic reflections were indexed with a commensurate propagation vector $\vec{k}_{\rm com} = (0.5,0.5,0.5)$ that corresponds to an up-up-down-down magnetic arrangement along the chains, which can be explained by a dominating next-nearest-neighbor magnetic interaction within the chains.

In this article, we present a comprehensive investigation of the magnetic properties of $NaFe(WO_4)_2$ in zero field and in magnetic fields applied along the monoclinic axis $\vec{b}$ by combining various macroscopic and neutron diffraction techniques on single crystals. We show that the zero-field magnetic structure is more complex than previously proposed [16], because it develops an incommensurate spin spiral, which, however, does not result in a multiferroic phase. Most interestingly, there are several phase transitions associated with the emergence of anharmonic components, whose signatures in some macroscopic properties (thermal expansion) are even larger than those associated with the onset of magnetic order in zero magnetic field.

II. SYMMETRY ANALYSIS

The magnetic symmetry of the system has been derived by applying representation analysis [18]. The crystallographic structure of $NaFe(WO_4)_2$ can be described in the space group $P2/c$ (No. 13). The magnetic Fe^{3+} ions are located at the special Wyckoff site 2*e* at $(0,0.670,1/4)$, which has twofold symmetry.

Nyam-Ochir *et al.* were able to describe the magnetic neutron powder data with a commensurate propagation vector of $\vec{k}_{\rm com} = (0.5,0.5,0.5)$ [16]. The corresponding little group $G_{\vec{k}_{\rm c}}$ is identical to the space group $P2/c$. It contains one two-dimensional irreducible representation Γ_1. In the case of the commensurate propagation vector, $\vec{k}_{\rm c}$ and $-\vec{k}_{\rm c}$ are equivalent and the star of $\vec{k}_{\rm c}$ consists of one vector. The character table and the corresponding symmetry conditions for the magnetic moments are given in Table I. The two-dimensional representation allows the two symmetry-connected moments in the crystallographic unit cell to be either collinear or canted. For a given moment (u,v,w), the second moment in the unit cell can align according to the four possibilities: (u,v,w), $(u,\bar{v},w)$, $(\bar{u},v,\bar{w})$, and $(\bar{u},\bar{v},\bar{w})$. The low-temperature commensurate magnetic structure AF1 in $MnWO_4$ is also described by this little group [19].

Neutron diffraction studies on a single crystal of $NaFe(WO_4)_2$ reveal an incommensurate magnetic propagation vector of the form $\vec{k}_{\rm ic} = (\delta_H,0.5,\delta_L) = (0.485,0.5,0.48)$ (see Sec. V B). Note, however, that this incommensurate vector is very close to $(0.5,0.5,0.5)$, so that the magnetic structure still

TABLE I. Character table and symmetry conditions of the little group $G_{\vec{k}_{\rm c}} = P2/c$, $\vec{k}_{\rm com} = (0.5,0.5,0.5)$.

	1	2	$\bar{1}$	*c*	(x,y,z)	$(\bar{x},\bar{y},\bar{z})$
Γ_1	1 0 0 1	1 0 0 −1	0 1 1 0	0 1 −1 0	(u,v,w)	(p,q,r)

TABLE II. Character table and symmetry conditions of the little group $G_{\vec{k}_{\rm ic}} = Pc$, $\vec{k}_{\rm ic} = (\delta_H, 0.5, \delta_L)$ with $a = e^{-i2\pi\cdot\delta_L\cdot r_z} = e^{-i2\pi\cdot 0.24}$.

	1	c	(x,y,z)	$(x,\bar{y},z+1/2)$	superspace symmetry
Γ_1	1	$-a$	(u,v,w)	$a\cdot(u,\bar{v},w)$	u,w imaginary, v real
Γ_2	1	a	(u,v,w)	$a\cdot(\bar{u},v,\bar{w})$	u,w real, v imaginary

locally resembles the up-up-down-down sequence shown in Fig. 1(b).

With the incommensurability along $\vec{a}^*$ and $\vec{c}^*$ the little group of the magnetic structure changes to $G_{\vec{k}_{\rm ic}} = \{1,c\}$. It contains two one-dimensional irreducible representations $\Gamma_{1,2}$. The character table and the corresponding symmetry conditions for the magnetic moments are given in Table II. In the case of the incommensurate propagation vector, $\vec{k}_{\rm ic}$ and $-\vec{k}_{\rm ic}$ are not equivalent and the star of $\vec{k}_{\rm ic}$ contains two vectors. Because the c glide plane connects the two Fe sites in the unit cell and since c belongs to $G_{\vec{k}_{\rm ic}}$, both sites thus belong to one orbit and can be described by three complex parameters u,v,w; cf. Table II. The incommensurate magnetic structures AF2 and AF3 of $\mathrm{MnWO_4}$ are also described in this little group [19].

The two irreducible representations Γ_1 and Γ_2 are thus described by three complex amplitudes u,v,w, whose six independent parameters can be reduced to five by arbitrarily choosing one phase, e.g., $u = |u|$. Further insight can be gained by magnetic superspace symmetry analysis, which takes into account additional symmetry elements not keeping $\vec{k}_{\rm ic}$ invariant [20]. The superspace analysis yields further constraints to the five remaining parameters of each symmetry by fixing the phases; see Table II [21]. Because u and w always have the same phase that differs from that of v by $\pm\frac{\pi}{2}$, a spiral magnetic structure emerges at each of the two Fe sites, but these two spirals have opposite chirality, which will be essential for the understanding of the absence of a multiferroic phase; see below.

III. EXPERIMENTAL METHODS

The macroscopic and microscopic properties presented in this article were measured on single crystals of $\mathrm{NaFe(WO_4)_2}$. The crystals were grown from sodium poly-tungstate flux [starting ratio $\mathrm{Na_2W_2O_7} : \mathrm{NaFe(WO_4)_2} = 3:2$, with excess of $\mathrm{WO_3}$] by the top seeded solution growth technique within the temperature range from 1172 to 1163 K. During typical growth periods of four weeks, dark green single crystals of up to 1 $\mathrm{cm^3}$ volume and well-developed morphology were obtained. The neutron scattering experiments have been performed on two samples of sizes $13\times 8\times 2$ $\mathrm{mm^3}$ and $6\times 7\times 2$ $\mathrm{mm^3}$, respectively. Macroscopic measurements were performed on smaller pieces of the same batch.

The magnetization was measured using a commercial superconducting quantum interference device (SQUID) magnetometer as a function of temperature from 1.8 to 300 K in magnetic fields up to 7 T applied along the principal crystallographic directions of the crystals. The specific heat (c_p) was measured by the thermal relaxation time method using a home-built calorimeter. The temperature- and magnetic-field-dependent length changes $\Delta L_b(T,B)$ were measured with a home-built capacitance dilatometer along the b axis. By numerically deriving the relative length changes with respect to temperature or magnetic field, the thermal-expansion ($\alpha = 1/L_b^0\,\partial\Delta L_b/\partial T$) or magnetostriction ($\lambda = 1/L_b^0\,\partial\Delta L_b/\partial B$) coefficients are obtained. The calorimeter (dilatometer) was attached to the ^{3}He pot in the high-vacuum chamber of a ^{3}He cryostat and c_p (ΔL_b) was measured in the temperature range from about 300 mK to 10 K in magnetic fields up to 17 T applied along the monoclinic b axis of the single-crystalline samples.

Neutron diffraction experiments have been performed at different instruments. The crystal and magnetic structure was investigated at the four-circle diffractometer D10 (ILL, Grenoble) at 12 K and 1.75 K, respectively. The Q and temperature dependence of the magnetic propagation vector was studied at the triple-axis spectrometers IN3 and IN14 (both ILL, Grenoble) using different crystal orientations. Finally, the high-field phases in magnetic fields applied along $\vec{b}$ were investigated at the four-circle diffractometer 6T2 with the lifting counter and vertical cryomagnet (LLB, Saclay).

IV. MACROSCOPIC MEASUREMENTS

A. Magnetization

Figures 2(a)–2(c) show the magnetic susceptibility of $\mathrm{NaFe(WO_4)_2}$ along the principal crystallographic directions measured on a single crystal. The high-temperature part was fitted by the inverse Curie-Weiss function $\chi_{\rm m}^{-1} = C^{-1}(T+\theta)$ yielding Weiss temperatures θ ranging from about -6.8 to -8.9 K depending on the field direction, see Fig. 2(b), and an average effective magnetic moment $\mu_{\rm eff,exp} = 5.93\,\mu_{\rm B}$, in very good agreement with the expected value of

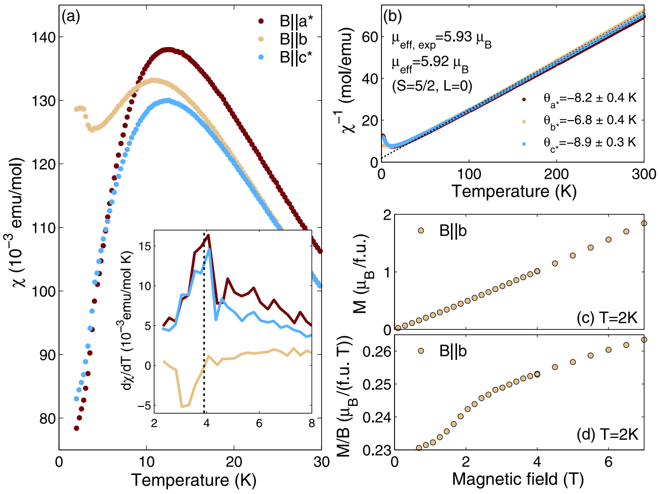

FIG. 2. Magnetic susceptibility of $\mathrm{NaFe(WO_4)_2}$ along principal crystallographic directions: (a) low-temperature behavior and (b) Curie-Weiss fit to the high-temperature part. The inset in (a) shows the derivative of the susceptibility with respect to the temperature. A magnetic field of 0.1 T was applied to the sample. (c) Magnetization on $\mathrm{NaFe(WO_4)_2}$ for magnetic fields applied along $\vec{b}$ on decreasing fields. (d) Magnetization per applied magnetic field along the same direction.

$\mu_{\text{eff}} = 2\sqrt{S(S+1)}\,\mu_{\text{B}} = 5.92\,\mu_{\text{B}}$ for a spin-only moment of Fe^{3+} with $S = 5/2$. The results agree with values determined from powder samples [16].

An expanded view of the low-temperature range of the susceptibility is shown in Fig. 2(a). All three $\chi(T)$ curves show broad maxima around 14 K, which signal the occurrence of strong magnetic correlations in the temperature range well above the transition temperature $T_{\text{N}} \simeq 3.9$ K where long-range magnetic order sets in. This value of T_{N} is obtained from the extrema of the temperature derivatives of $\chi(T)$ and is indicated by a dashed line in the inset of Fig. 2(a). The occurrence of strong magnetic correlations above T_{N} is typical for low-dimensional magnetic systems and is naturally expected for $\text{NaFe(WO}_4)_2$, which consists of two-dimensional layers of magnetic Fe^{3+} spin chains that are weakly coupled along the perpendicular direction $\vec{a}$.

Below T_{N}, the susceptibilities for fields along $\vec{a}*$ and $\vec{c}*$ further decrease, whereas $\chi_b(T)$ even slightly increases. This anisotropic behavior already starts near the maxima of $\chi_i(T)$, i.e., well above T_{N}, and it indicates that the magnetic moments are preferentially aligned perpendicular to the b axis. As will be seen below, within the ac planes, the magnetic moments align approximately along the axis bisecting $\vec{a}*$ and $\vec{c}*$, which explains the very similar temperature dependencies of χ_i for magnetic fields applied along these two directions.

Finally, in Fig. 2(c) we show the induced magnetization for fields up to $B = 7\ \text{T} \parallel \vec{b}$. The magnetization almost linearly increases with field and reaches about $2\ \mu_{\text{B}}/\text{f.u.}$, i.e., about 40% of the expected saturation magnetization of the $S = 5/2$ spin moments of Fe^{3+}. However, a closer inspection of the magnetization per field [cf. Fig. 2(d)] reveals an anomaly at about 2 T indicating a magnetic reorientation, which will be discussed in detail below.

B. Specific heat

The specific heat of $\text{NaFe(WO}_4)_2$ measured at low temperatures is displayed in Fig. 3(a) for different magnetic fields applied along $\vec{b}$. In general, the values were determined during a heating run by stepwise heating the sample (red data points). In addition, we measured c_p for various fields also during a cooling run by successively decreasing the base temperature (black data points), but in none of these measurements a clear temperature hysteresis could be resolved.

In zero field and in 1 T, the specific heat shows a rather broad maximum in $c_p/T = \partial S/\partial T$ at 4 K signaling an inflection point of the temperature dependence of the (magnetic) entropy. This feature corresponds nicely to the magnetic transition temperature $T_{\text{N}} \simeq 3.9$ K as determined from the magnetization. However, the weakness of this feature also reveals that instead of a sharp transition the 3-dimensional correlations develop rather gradually in $\text{NaFe(WO}_4)_2$. Again, this behavior can be naturally explained by the weakly coupled 2-dimensional magnetic planes in $\text{NaFe(WO}_4)_2$. Upon lowering the temperature, the in-plane magnetic correlations continuously evolve such that the magnetic entropy continuously freezes already well above T_{N}, and the 3-dimensional ordering only causes a weak additional decrease of magnetic entropy.

Above 2 T, the feature at the transition temperature sharpens significantly and its shape indicates a first-order phase transition, but as already mentioned there is essentially no temperature hysteresis detectable. Moreover, the total entropy change in the temperature range from 0.3 to 10 K [see Fig. 3(b)] only amounts to about 60% of the expected full magnetic entropy $S_{\text{mag}} = N_{\text{A}} k_{\text{B}} \ln(2S+1) \simeq 14.9\ \text{J/(mol K)}$ of an $S = 5/2$ system. In fact, this total entropy change hardly varies from zero field up to 6 T, although the entropy decrease at the transition sharpens up above 2 T. For all fields studied, this entropy change remains below 20% of the expected total magnetic entropy, which once again emphasizes the importance of short-range correlations persisting well above T_{N}. Above 8 T, the total entropy change and the transition temperature systemically decrease with further increasing field and the antiferromagnetic order is fully suppressed above about 15 T.

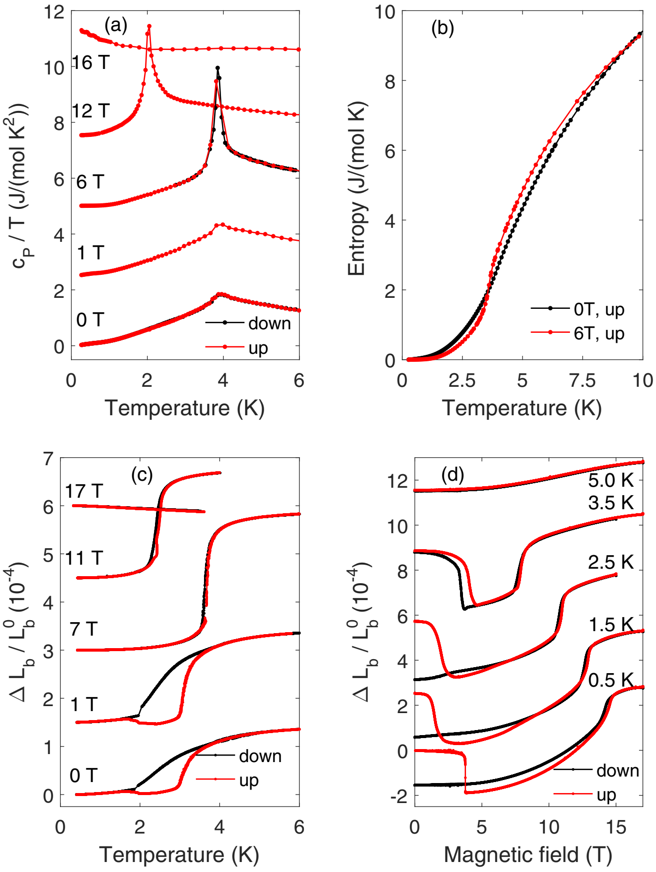

FIG. 3. Specific heat (a), entropy (b), thermal expansion (c), and magnetostriction (d) of $\text{NaFe(WO}_4)_2$ for magnetic fields applied along $\vec{b}$. The length changes in (c) and (d) were measured along the monoclinic axis $\vec{b}$. The specific-heat and thermal-expansion data were obtained upon decreasing and increasing temperature (black and red curves, respectively). For the magnetostriction, the sample was cooled in zero field before the field was increased and decreased at constant temperature (red and black curves, respectively). The curves are separated by a constant offset: (a) $2.5 \times 10^{-4}\ \text{J/(mol K}^2)$, (c) 1.5×10^{-4}, and (d) 2.5×10^{-4}.

C. Thermal expansion and magnetostriction

Figures 3(c) and 3(d) show the thermal expansion and magnetostriction of $\text{NaFe(WO}_4)_2$ along the monoclinic axis $\vec{b}$

for magnetic fields applied along the same direction. Because of the very strong magnetoelastic effects of the order of 10^{-4} the relative length changes $\Delta L_b(T,B)/L_b^0 = \frac{\Delta b}{b}$ are displayed here instead of the corresponding temperature or field derivatives α or λ. All curves were measured upon continuously increasing (red lines) and decreasing (black lines) either the temperature at constant B or the field at constant T. In magnetic fields above 2 T, the thermal-expansion measurements confirm some of the basic observations from the specific-heat measurements. The phase transitions cause very large and sharp changes of $\Delta L_b(T)/L_b^0$, whose shape and magnitude are typical for first-order phase transitions, but no systematic temperature hysteresis is present in this field range.

For zero field and in 1 T, however, the thermal-expansion data reveal a systematically different behavior compared to the $c_p(T)$ measurements. Upon cooling, $\Delta L_b(T)$ continuously decreases down to about 2 K, but then the slope abruptly changes to a moderate decrease of $\Delta L_b(T)$ upon further cooling to the minimum temperature of 300 mK. In the heating run, $\Delta L_b(T)$ reversibly follows the cooling curve only up to about 1.8 K. Then, on further heating, $\Delta L_b(T)$ first shows a broad minimum around 2.5 K, which is followed by an abrupt steep increase at 3 K and around 3.5 K the heating curve of $\Delta L_b(T)$ finally meets the previous cooling curve and no further hysteresis is observed. Most surprisingly, the hysteresis and the anomalies of the low-field thermal expansion are observed in a temperature range where the corresponding $c_p(T)$ curves are fully reversible without any anomalies. In contrast, in the thermal-expansion data no anomaly shows up at the Néel temperature $T_N \simeq 4$ K. As will be discussed below, this is related to the fact that an incommensurate, anharmonic low-field phase develops in NaFe(WO$_4$)$_2$ and $\Delta L_b(T)$ scales with both the variation of incommensurability and with the anharmonicity of magnetic order.

The magnetostriction $\Delta L_b(B)$ measured after zero-field cooling is displayed for selected temperatures in Fig. 3(d). At 0.5 K, a large discontinuous contraction of $\Delta L_b(B)$ takes place at $B_{c1}^{\mathrm{up}} \simeq 3.8$ T, which is followed by a continuous expansion up to about $B_{c2}^{\mathrm{up}} \simeq 14.5$ T where an abrupt expansion occurs and above 15 T a saturation of $\Delta L_b(B)$ sets in. With decreasing field, the upper transition is shifted by $\simeq$0.3 T towards lower fields and reverses the abrupt length change, whereas the lower transition is absent. On increasing temperature, the abrupt length change at the upper transition systematically increases, whereas the transition field and the hysteresis width decrease to $B_{c2}^{\mathrm{up}} \simeq 9.7$ T and $B_{c2}^{\mathrm{up}} - B_{c2}^{\mathrm{down}} \simeq 0.1$ T, respectively, at $T = 3$ K. The magnetostriction anomalies at the upper transition well agree with the corresponding anomalies of the thermal-expansion and the specific-heat data in the (B,T) plane and reveal that the magnetic-ordering transition of NaFe(WO$_4$)$_2$ in finite magnetic fields is a first-order transition and that this antiferromagnetic order is fully suppressed above about 15 T. The absence/presence of the lower transition reveals that there are metastable phases in the low-field low-temperature range. The field range of these metastable phases shrinks with increasing temperature and seems to vanish around 3 K, where the magnetostriction $\Delta L_b(B)$ indicates a first-order low-field transition with a pronounced hysteresis $B_{c1}^{\mathrm{up}} - B_{c1}^{\mathrm{down}} \simeq 1$ T. Note, however, that $\Delta L_b(B)$ is not fully reversible at this transition and, moreover, additional hysteresis effects are also present in $\Delta L_b(B,T)$ over a wider field and temperature range. These effects most probably arise from coexisting phases due to incomplete first-order transitions.

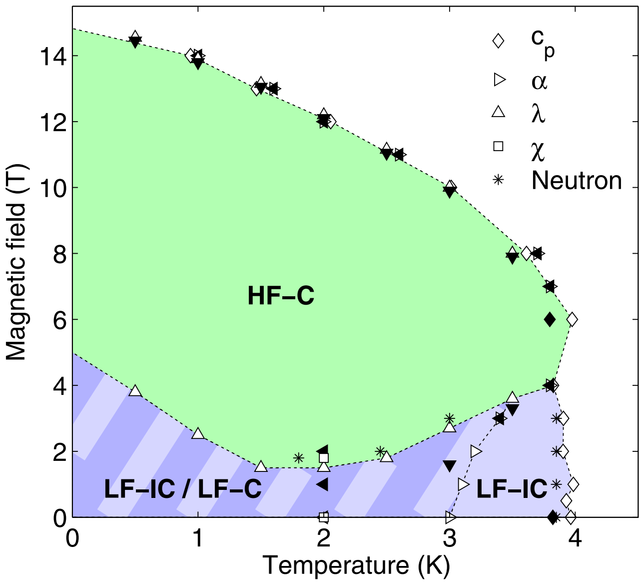

FIG. 4. Magnetic phase diagram of NaFe(WO$_4$)$_2$ for applied magnetic field along $\vec{b}$. The transition temperatures derived from measurements of the specific heat (c_p), thermal expansion (α), magnetostriction (λ), magnetization (χ), and neutron diffraction are indicated upon heating (open symbols) and cooling (filled symbols). We distinguish three different phases: low-field incommensurate (LF-IC), low-field commensurate (LF-C), and high-field commensurate (HF-C).

D. Phase diagram

The basic features of the magnetic phase diagram of NaFe(WO$_4$)$_2$ are summarized in Fig. 4. Open and filled symbols denote transition fields or temperatures that were obtained from the anomalies of the various macroscopic quantities (χ, c_p, α, λ), either upon increasing or decreasing the magnetic field or temperature, respectively. In addition, important microscopic information is included that is obtained from the neutron diffraction measurements, which will be discussed below. The ordered phases of NaFe(WO$_4$)$_2$ cover a field and temperature range below about 4 K and 15 T, which can be divided into three different regions. Above about 4 T, there is a high-field ordered phase HF-C with commensurate magnetic order, whereas the low-field region further splits into two regions. Below about 3 K, there are two low-field phases LF-IC and LF-C with incommensurate and commensurate magnetic order, respectively. The LF-IC phase is reached upon zero-field cooling, while the LF-C phase is observed after successively ramping the magnetic field up and down at low temperature. In the temperature range between 3 and 4 K, another incommensurate low-field phase LF-IC* is found, that differs from the LF-IC phase by the absence of a strong anharmonic modulation; see below.

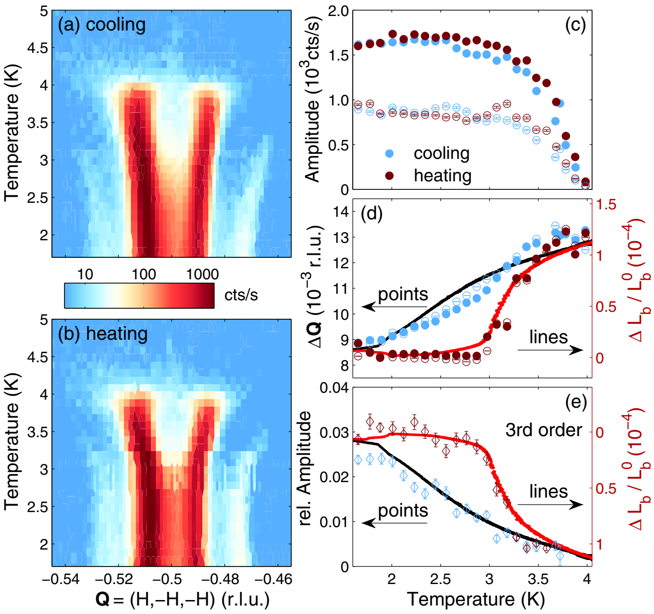

FIG. 5. Magnetic phase transition in NaFe$(WO_4)_2$ upon cooling and heating at IN3. (a), (b) Intensity mapping of $\vec{Q}$ scans along the position of the magnetic Bragg peak $\vec{Q} = (-0.5,0.5,0.5)$ upon cooling and heating through the phase transition. The color is logarithmically coded. Gaussian peaks were fitted to the data. (c) Peak intensities of both magnetic satellites (open and closed markers, respectively). (d) Positions of the satellites relative to the commensurate Bragg point. (e) Relative peak intensity of the incommensurate third-order signal upon heating and cooling. The onset of the third-order reflections coincides with the modulation of the propagation vector. The temperature dependence in (d) and (e) is compared to the thermal-expansion data in zero field [black and red lines from Fig. 3(c)].

V. MICROSCOPIC MEASUREMENTS

A. Zero-field temperature dependence

The temperature dependence of the magnetic superstructure reflections was investigated by neutron diffraction at IN3. We worked with a fixed neutron energy of 14.7 meV ($k_f = 2.66\,\text{Å}^{-1}$) and a sample orientation of [1,0,0]/[0,1,1]. Figures 5(a) and 5(b) show intensity maps of $\vec{Q}$ scans along [1,1,1] over the magnetic satellites at $\vec{Q} = (-0.5,0.5,0.5)$ upon cooling and heating. At about 4 K, two strong incommensurate Bragg peaks develop whose positions are temperature dependent. The magnetic satellites are accompanied by weak third-order reflections and a weak signal at the commensurate Bragg peak position. Well above the transition temperature, strong diffuse scattering persists in agreement with the low-dimensional character deduced from the macroscopic measurements. Three Gaussian functions were fitted to the data to take into account the intensities at the two incommensurate positions and the commensurate position in the center. The signal at the commensurate Bragg position is weak in comparison to the incommensurate peaks but cannot be attributed to $\lambda/2$ contamination from a structural peak since its intensity varies with temperature. A detailed analysis of this finding is limited by the weakness of the signals and because the magnetic satellites are so close to each other. This is an essential difference to $MnWO_4$ where the incommensurate magnetic modulation is much farther away from the commensurate value. Anharmonic components were also observed in the AF2 phase of $MnWO_4$ [22] and there they are related with magnetoelectric memory effects observed for the electric-field control of multiferroic domains [23,24].

The appearance of the third-order reflections must be attributed to an anharmonic perturbation of the incommensurate structure. A deformed sinusoidal wave can be described by additional wave vectors in the Fourier transformation. Higher-order harmonics often indicate a squaring-up of the magnetic structure. This is an expected feature at low temperatures as an incommensurate sinusoidal spin-density wave cannot be the ground state of a local moment system [25]. The ratio of third- and first-order satellites is $I_{3\text{rd}}/I_{1\text{st}} \approx 3\%$ in NaFe$(WO_4)_2$. Figure 5(c) shows the temperature dependence of the fitted peak intensity of the first-order satellites. The rapid growth in intensity below about 3.8 K signals the development of long-range magnetic order, in good agreement with the Néel temperature $T \simeq 3.9\,\text{K}$ derived from the susceptibility and specific-heat measurements.

In Fig. 5(d), the fitted peak positions of the first-order magnetic satellites are shown for the cooling and heating cycles. Note that here the distance ΔQ to the commensurate position is plotted. Both first-order satellites show the same behavior within a cycle, but the temperature dependence is different for heating and cooling. Upon cooling, the incommensurability ΔQ decreases continuously with decreasing temperature, while upon heating, ΔQ remains constant up to 3.0 K and increases rapidly at higher temperatures. An analogous temperature hysteresis is seen in the temperature dependence of the third-order magnetic satellites; see Fig. 5(e) where the relative intensities $I_{3\text{rd}}/I_{1\text{st}}$ are plotted.

The temperature hysteresis of ΔQ and $I_{3\text{rd}}/I_{1\text{st}}$ remarkably resembles the temperature hysteresis observed in the zero-field thermal-expansion data $\Delta L_b(T)$, which is included in Figs. 5(d) and 5(e). In contrast, the onset of incommensurate harmonic order at T_N has no magnetoelastic impact on the b lattice parameter. In most magnetoelastic materials [26–30], anomalies in the strain are coupled to the order parameter, typically the (staggered) magnetic moment, and thus appear just at T_N, while the situation in NaFe$(WO_4)_2$ is more complex. In NaFe$(WO_4)_2$, the change in the lattice is not proportional to a power of the averaged ordered moment, $\langle |m| \rangle$, but to the emergence of anharmonicity either in the incommensurate phase or in the commensurate order. A semiquantitative analysis of the magnetoelastic coupling will be given in Sec. VI after the discussion of the commensurate magnetic structures.

B. Propagation vector

In order to investigate the precise value of the incommensurate magnetic propagation vector along the principal crystallographic directions, different crystal orientations had been used in neutron diffraction. At IN14, we worked with a neutron energy of 3.5 meV ($k = 1.3\,\text{Å}^{-1}$) and a sample orientation of [1,1,0]/[0,0,1]. At IN3, we worked with an neutron energy of 14.7 meV ($k = 2.66\,\text{Å}^{-1}$) and a sample orientation of [1,0,1]/[0,1,0] and [1,0,0]/[0,1,1]. Figures 6(a)–6(c) show two-dimensional intensity maps of $\vec{Q}$

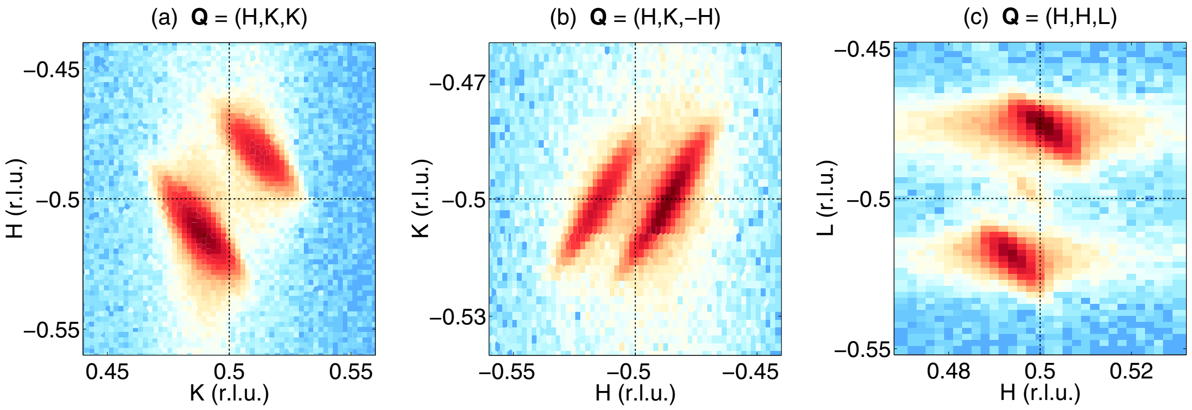

FIG. 6. Intensity mapping of $\vec{Q}$ scans along magnetic Bragg peaks of NaFe(WO$_4$)$_2$ at 3.8 K in three different orientations: (a) $\vec{Q} = (-0.5,0.5,0.5)$ in [1,0,0]/[0,1,1], (b) $\vec{Q} = (-0.5,-0.5,0.5)$ in [0,1,0]/[1,0,1], and (c) $\vec{Q} = (0.5,0.5,-0.5)$ in [0,0,1]/[1,1,0]. The color is logarithmically coded. The intersection of dashed lines indicates the commensurate Bragg peak position.

scans along two magnetic satellites in NaFe(WO$_4$)$_2$ in three different crystal orientations at 3.8 K. The intersection of dashed lines indicates the commensurate peak position. This temperature is slightly below the magnetic transition temperature, where the splitting of the satellites is most pronounced. The intensity is logarithmically coded and diffuse scattering is visible around the static Bragg peaks. The images are two-dimensional cuts through the three-dimensional $\vec{Q}$ space. In Fig. 6(a), the single crystal was oriented along [1,0,0]/[0,1,1] and was measured at the spectrometer IN3. The splitting of the incommensurate magnetic satellites occurs along both axes of the scattering plane. The splitting along [1,0,0] is $2\Delta_H \approx 0.03$. Figure 6(b) was recorded at IN3 in the scattering plane [0,1,0]/[1,0,1]. In this orientation the splitting is only present along [1,0,1]. Within the experimental precision we cannot determine a splitting along the monoclinic axis, $\Delta_K = 0$. Finally at the spectrometer IN14 the crystal was oriented along [0,0,1]/[1,1,0]. The splitting is again present along both axes and we obtain $2\Delta_L \approx 0.04$ for the incommensurability along $\vec{c}^*$.

We can conclude that the incommensurate splitting of the magnetic propagation vector in the zero-field phase of NaFe(WO$_4$)$_2$ only occurs perpendicular to the monoclinic axis $\vec{b}$. This is a symmetry plane of the Brillouin zone for the space group $P2/c$. The propagation vector at 3.8 K is $\vec{k}_{\text{inc}} = (0.485,0.5,0.48)$.

C. Diffuse scattering

We will continue with the investigation of the temperature and $\vec{Q}$ dependence of the diffuse scattering in the paramagnetic phase of NaFe(WO$_4$)$_2$. The experiment was performed at the spectrometer IN3 using a single crystal of NaFe(WO$_4$)$_2$ in the orientation [1,0,0]/[0,1,1]. Figures 7(a) and 7(b) show two-dimensional intensity maps along the commensurate Bragg peak $\vec{Q} = (-0.5,0.5,0.5)$ at 4.0 K and 4.2 K, slightly above the ordering temperature. At 4.0 K, the diffuse scattering is well centered around the incommensurate Bragg peak positions. The signal is rather sharp along [0,1,1] and significantly broadened along [1,0,0]. At 4.2 K this situation is even more pronounced. The diffuse scattering remains centered at the commensurate value along [0,1,1] and is nearly constant along the a^* axis.

Figure 7(c) shows $\vec{Q}$ scans along [0,1,1] over the commensurate Bragg peak position $\vec{Q} = (-0.5,0.5,0.5)$ at different temperatures above the magnetic transition. Diffuse scattering is present up to 6 K, which is 1.5 times larger than the transition temperature of $T_N = 3.9$ K suggesting a low-dimensional or

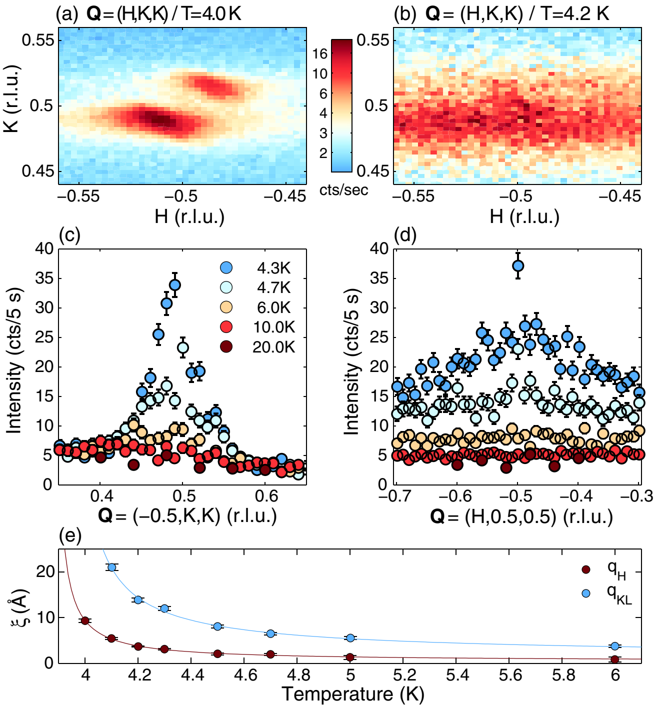

FIG. 7. Diffuse scattering in NaFe(WO$_4$)$_2$. Two-dimensional intensity mapping of $\vec{Q}$ scans around $\vec{Q} = (-0.5,0.5,0.5)$ upon heating through the phase transition in the orientation [1,0,0]/[0,1,1] at (a) 4.0 K and (b) 4.2 K, slightly above $T_N = 3.9$ K at IN3. The color is logarithmically coded. Panels (c) and (d) show $\vec{Q}$ scans through the commensurate Bragg position along [0,1,1] and [1,0,0] at several temperatures. Diffuse magnetic scattering is present up to 6 K. (e) Correlation length ξ determined by Lorentzian fits for both directions. A power-law function $\xi \propto (T - T_N)^{\nu}$ was fitted to the data.

frustrated character of the system. This finding is in perfect agreement with the macroscopic measurements presented in Sec. IV. Magnetic resonance studies on NaFe(WO$_4$)$_2$ also revealed a two-dimensional character of the magnetic order and the ratio of intralayer J to interlayer exchange J' was estimated to be $J' \approx 10^{-6}J$ [31].

We now focus on the anisotropy of the magnetic correlations. Figure 7(d) shows the temperature dependence of $\vec{Q}$ scans along [1,0,0]. The diffuse scattering is significantly broadened along this direction. By fitting the data with a Lorentzian function, one can determine the correlation length of the diffuse order. The finite instrument resolution can be neglected in the investigated temperature range because the diffuse signal is significantly broadened.

The temperature dependence of the correlation length along both directions is shown in Fig. 7(e). NaFe(WO$_4$)$_2$ crystallizes in a layered structure with separated planes of Na, Fe, and W parallel to the *bc* plane (see Fig. 1 and Ref. [17]). The distance of the magnetic ions along $\vec{a}*$ is almost 10 Å. The resulting weakness of the coupling along $\vec{a}*$ is visible in the two-dimensional diffuse scattering in the paramagnetic phase. Correlations between the magnetic moments first occur below 10 K inside the *bc* planes, where the magnetic moments form closely neighboring zigzag chains. Only at lower temperatures the system develops 3-dimensional correlations between the planes.

D. Magnetic and nuclear structure at zero field

The crystal and magnetic structure of NaFe(WO$_4$)$_2$ was investigated at D10. Two single crystals ($13 \times 8 \times 2$ mm^3 and $6 \times 7 \times 2$ mm^3) were used for the experiment. The D10 diffractometer was equipped with a 80×80 mm^2 microstrip area detector and two wavelengths, 1.26 Å and 2.36 Å, were used. Magnetic Bragg reflections were recorded at 1.75 K and structural Bragg reflections were recorded at 12 K, well above the magnetic phase transition. The magnetic propagation vector $\vec{k}_{\text{inc}} = (0.485,0.5,0.48)$ of NaFe(WO$_4$)$_2$ is incommensurate. However, the resolution of D10 is insufficient to separate the two satellites corresponding to $\vec{k}_{\text{ic},1} = (0.485,0.5,0.48)$ and $\vec{k}_{\text{ic},2} = (-0.485,0.5,-0.48)$. The collection of magnetic peaks has been done by long scans at the positions in Q space generated by the commensurate propagation vector. The structure refinement was done in the space group $P2/c$ with the lattice parameters given in the introduction using the program FULLPROF [32]. The data sets from both single crystals yield quantitatively the same results and we will present only the results from the more complete data set.

Structural reflections were recorded at 12 K in the paramagnetic phase. At a neutron wavelength of 1.26 Å, a total of 766 reflections were collected. For the refinement 367 independent nuclear reflections were used. The internal and weighted R values are 1.64% and 1.83%, respectively (on the intensity). The results of the refinement of the structural parameters are given in Table III. Isotropic temperature factors and anisotropic extinction correction (model 4 in FULLPROF [32]) were applied. The values for the atomic positions correspond very nicely to the results obtained from powder data [16] and the anisotropic extinction parameters reflect the platelike shape of the crystal.

TABLE III. Structural parameters of NaFe(WO$_4$)$_2$ at 12 K in the space group $P2/c$, with $a = 9.88$ Å, $b = 5.72$ Å, $c = 4.94$ Å, and $\beta = 90.33$. The data were recorded at the diffractometer D10 and the refinement was done using FULLPROF [32]. $R_{F^2} = 3.70$, $R_{wF^2} = 3.55$, $R_F = 2.87$, and $\chi^2(I) = 4.13$.

	x	y	z	U_{iso} (Å^2)
Fe	0.0	0.67074(19)	0.25	0.04(2)
Na	0.5	0.6971(6)	0.25	0.35(5)
W	0.23704(14)	0.1831(2)	0.2572(3)	0.12(3)
O1	0.35385(12)	0.3813(3)	0.3816(3)	0.25(3)
O2	0.10888(13)	0.6226(3)	0.5923(3)	0.22(2)
O3	0.33177(13)	0.0897(2)	0.9533(3)	0.22(3)
O4	0.12606(13)	0.1215(3)	0.5757(3)	0.17(2)

The structural data set can also be used to verify the occupation of the different atomic sites. It was mentioned before that the mechanism of the magnetic coupling along the extended a axis is still unclear. The coherent neutron scattering lengths of sodium and iron are $b_{\text{Na}} = 3.63$ fm and $b_{\text{Fe}} = 9.45$ fm, respectively, which renders a differentiation of both elements possible. The refinement with FULLPROF [32] yields a deviation of only 1% to 2% per site. The layered structure is thus well ordered and an influence of mixed occupation on the magnetic structure can be *a priori* excluded.

Magnetic Bragg reflections were recorded at 2 K in the ordered phase. At a neutron wavelength of 1.26 Å, a total of 423 reflections were collected. A total of 411 independent magnetic reflections were used for the refinement. As mentioned above, the incommensurate satellites could not be measured independently at D10. Instead, we used the commensurate propagation vector to measure the magnetic reflections and integrated over both incommensurate peaks. The refinement program FULLPROF [32] allows us to treat the list of measured intensities in a way that the contribution of two neighboring magnetic satellites is summed up in clusters and the incommensurate propagation vector could be used for the refinement.

Different models were used to describe the data. The two sites were described by identical Fourier coefficients and the phase shift $\phi_{\vec{k}_c}$ arising from the different z values. A comparison of the refinements using different models is given in Table IV. The previous analysis of neutron powder data yielded a model with a commensurate propagation vector

TABLE IV. Residual values for the refinements of the magnetic reflections of NaFe(WO$_4$)$_2$ taken at 2 K on D10 using different models. The commensurate (COM), spin-density-wave (SDW), and spiral models are explained in the text. For the spiral models, the major axes are along $\vec{e}_{ac}$ and $\vec{b}$. The best results are achieved assuming a spin spiral described by Γ_2.

	COM *a*	SDW *a*	SDW *ac*	SDW *abc*	spiral Γ_1	spiral Γ_2	spiral $\Gamma_1 + \Gamma_2$
R_{F^2}	47.8	47.9	15.0	14.9	12.2	11.7	15.1
R_{wF^2}	51.8	51.8	16.0	15.6	13.9	13.3	15.5
R_F	29.2	29.2	9.1	9.1	7.3	7.1	9.0
$\chi^2(I)$	239.0	240.0	22.7	22.1	10.9	9.9	21.6

and moments aligned antiparallel along $\vec{a}$ [16]. This model, however, is not compatible with the single-crystal data from the D10 diffractometer. The fit is improved by allowing the spins to rotate in the *ac* plane. Another minor improvement can be achieved when we allow an additional component along the monoclinic axis $\vec{b}$, that, however, remains small. This result agrees with the analysis of the magnetic susceptibility, which suggests a magnetic moment primarily ordered in the *ac* plane.

The fit results are similar for a collinear spin density wave (SDW) and a spin-spiral rotating in the $\vec{e}_{ac}$-$\vec{b}$ plane. The vector $\vec{e}_{ac}$ denotes the direction of the easy axis in the *ac* plane and has an angle of ≈48° with the *a* axis. Spin spirals with a different rotation axis are not compatible with the data.

We now take into account the full symmetry analysis for the case of an incommensurate propagation vector $\vec{k}_{\mathrm{ic},1} = (0.485,0.5,0.48)$; cf. Table II. Both Fe sites are connected by a glide plane *c* along the monoclinic axis and have a phase difference $\phi_{\vec{k}} = 2\pi \times 0.24$. The refinement gives the best result for an elliptical spin spiral with moments rotating in the $\vec{e}_{ac}$-$\vec{b}$ plane. This model is compatible with either of the two irreducible representations Γ_1 and Γ_2 and refining both models yields only slightly better reliability values for Γ_2, but the summation of neighboring magnetic satellites prohibits a clear differentiation. This Γ_2 model is displayed in Fig. 8 and it corresponds to the non-multiferroic AF3 phase in $\mathrm{MnWO_4}$ [21]. A combination of both representations constrained to identical chiral structures at both sides (only three independent parameters) clearly worsens the fit.

The difference of the spiral models, using either one or both irreducible representations, is the rotation of the two moments in the crystallographic unit cell relative to each other. When only one representation is applied, the moments rotate in the opposite sense, relative to each other. Only the combination of both representations allows the spirals to rotate along the same direction, which however is necessary in order to imply a finite ferroelectric polarization inverse Dzyaloshinskii-Moriya effect $\vec{D}_{ij} \times (\vec{S}_i \times \vec{S}_j)$ [33]. Such an arrangement is for example observed in the multiferroic AF2 phase in $\mathrm{MnWO_4}$ but not in $\mathrm{NaFe(WO_4)_2}$. This is in agreement with the absence of a pyroelectric current in $\mathrm{NaFe(WO_4)_2}$, which was reported recently [34]. A similar situation was discussed for the AF3 phase in $\mathrm{MnWO_4}$ applying the superspace formalism [21,35]. Urcelay-Olabarria *et al.* describe the AF3 structure as counter-rotating spirals, which prohibit the development of a ferroelectric polarization in this phase. Furthermore, also for Co-doped $\mathrm{Ni_3V_2O_8}$ such a compensation of spiral objects with opposite signs has been reported [36].

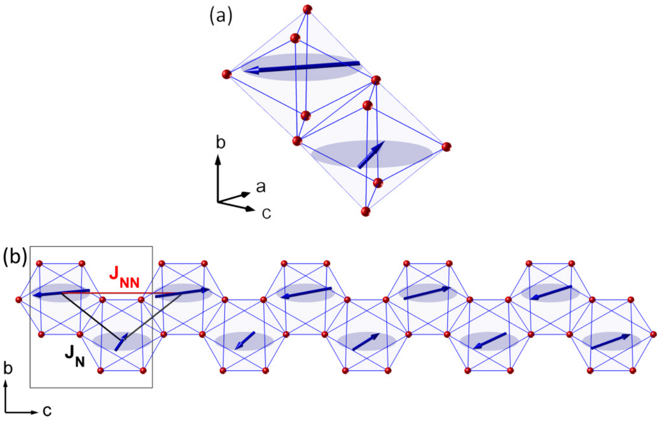

FIG. 8. Magnetic structure of $\mathrm{NaFe(WO_4)_2}$ at 2 K corresponding to Γ_2 as it is determined by single-crystal diffraction on D10: (a) Crystallographic unit cell with magnetic moments and oxygen ions and (b) evolution of the spiral along $\vec{c}$. The ellipses show the rotation plane of the magnetic moments with the principal axes $\vec{e}_{ac}$ and $\vec{b}$. Note that the spirals in the upper and lower rows rotate with opposite sense.

The lengths of the major and the minor principal axis of the elliptical spiral in Fig. 8 are $M_{\max} = \sqrt{(M_x^2 + M_z^2)} = 4.88(4)\,\mu_{\mathrm{B}}$ and $M_{\min} = M_y = 1.09(5)\,\mu_{\mathrm{B}}$, with a ratio $M_{\min}/M_{\max} = 0.22$. The angle between the major principal axis and the *a* axis is 47.7°. Given the strong deformation of the ellipse, the magnetic moments cannot order at every position in the lattice, similarly to the case of a spin-density wave. By comparing the area of the ellipsoid with a circle of the same area, one obtains an average oriented moment of about 3.5 μ_{B}, which is only 70% of the moment of $\mathrm{Fe^{3+}}$. Note, however, that the model described by FULLPROF [32] only accounts for the harmonic incommensurate spin spiral. The anharmonic squaring up which increases the ordered moment is are not taken into account in this model.

E. High-field phase

Finally, we investigate the high-field magnetic phase. The experiment was performed at 6T2 with a neutron wavelength of 2.35 Å. Figure 9(a) shows the intensity map of rocking scans along the magnetic Bragg peak position $\vec{Q} = (0.5,-0.5,-0.5)$ for magnetic fields applied along the monoclinic axis $\vec{b}$. The intensity is logarithmically color coded. The application of the magnetic field along the monoclinic axis strongly affects the incommensurate splitting of the satellites. At a magnetic field of about 1.2 T the satellites merge into one commensurate peak. The field was first increased to a maximum field of 5 T and then decreased to zero field at constant temperature.

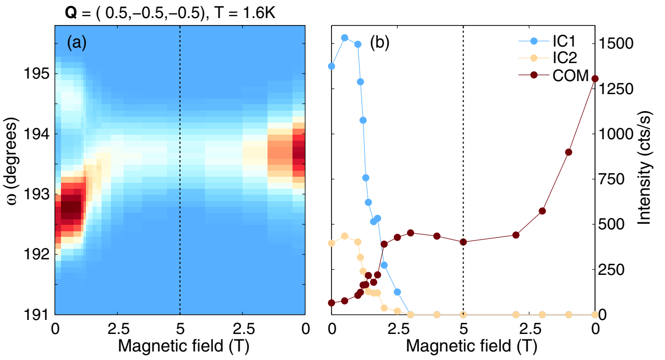

FIG. 9. Magnetic field dependence of the magnetic structure in $\mathrm{NaFe(WO_4)_2}$ at 6T2. (a) Intensity mapping of rocking scans along the magnetic Bragg peak position $\vec{Q} = (0.5,-0.5,-0.5)$ for increasing and decreasing magnetic field $B \parallel \vec{b}$ at 1.6 K. (b) Corresponding Bragg peak intensities of incommensurate (IC1 and IC2) and commensurate (COM) reflections fitted by Gaussian functions. Lines between points are a guide to the eye.

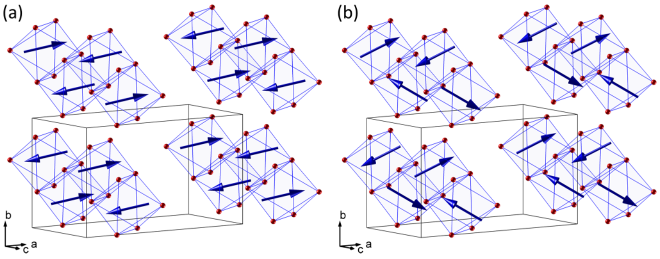

FIG. 10. Magnetic structures of $NaFe(WO_4)_2$ at 1.6 K as determined by single-crystal diffraction on 6T2 with magnetic fields applied along $\vec{b}$: (a) High-field commensurate phase at 5 T and (b) low-field commensurate phase at zero field. The induced ferromagnetic magnetization was not taken into account.

In decreasing fields, only a modulation of the intensity is visible and the scattered intensity remains at the commensurate position. Gaussian functions have been fitted to the data and resulting amplitudes are shown in Fig. 9(b). The first transition at 1.2 T perfectly matches the phase transition observed in the magnetostriction data [cf. Fig. 3(b)].

We can thus assign three different magnetic phases in $NaFe(WO_4)_2$ as shown in the phase diagram in Fig. 4: The system undergoes a phase transition from a paramagnetic towards a low-field incommensurate (LF-IC) magnetic structure with a propagation vector $\vec{k}_{\mathrm{inc}} = (0.485,0.5,0.48)$. In magnetic fields applied along $\vec{b}$, the propagation vector becomes commensurate $\vec{k}_{\mathrm{com}} = (0.5,0.5,0.5)$ and this phase is denoted as high-field commensurate (HF-C). Finally, the commensurate structure changes when the magnetic field decreases again which defines the low-field commensurate (LF-C) phase; see Fig. 4.

The results from the zero-field diffraction data will help to analyze the data collected in the high-field phase of $NaFe(WO_4)_2$. In addition to the temperature and magnetic field dependence of the propagation vector, 36 magnetic reflections were collected at 1.6 K in 0 T, 5 T, and again 0 T. The instrument was equipped with a cryomagnet, which cannot be used in combination with the Eulerian cradle. The movement of the sample was therefore limited to a rotation within the scattering plane. The installed lifting counter geometry allowed for the movement of the detector up to 30° perpendicular to the scattering plane in order to increase the accessible $\vec{Q}$ space. The small number of reflections and the absence of observed reflections along $\vec{b}$ limits the completeness of the data set. A precise refinement of the magnetic structure is not possible but the data gives significant information about the orientation of the moments in the different magnetic phases.

The 6T2 zero-field data confirm the model for the magnetic structure determined from the D10 data in the LF-IC phase. As a result we get the same incommensurate spin spiral with main axes along $\vec{e}_{ac}$ and $\vec{b}$, which can be described by one irreducible representation. The ratio between the components along $\vec{c}$ and $\vec{a}$ is $M_z/M_x \approx 1.1$, which corresponds to an angle of 47.7° to the a axis. A model of the magnetic structure is shown in Fig. 8(a).

Figure 10(a) shows a model of the magnetic structure determined from the 6T2 data in a magnetic field of 5 T applied along the monoclinic axis. The figure displays only the commensurate antiferromagnetic order without the induced ferromagnetic moment along $\vec{b}$ (see also Table V). The propagation vector of the HF-C phase changes to a commensurate $\vec{k}_{\mathrm{com}} = (0.5,0.5,0.5)$. The relative orientation of the spin at the second Fe^{3+} site in the crystallographic unit cell was determined by a comparison of four different configurations as described previously: $(\bar{u},\bar{v},\bar{w})$, $(\bar{u},v,\bar{w})$, $(u,\bar{v},w)$, and (u,v,w). The resulting R values (16%, 25%, 52%, and 96%, respectively) show that the best fit is obtained for the antiparallel alignment. The moments are collinear and antiferromagnetically ordered with components along all three axes: $M_x = 2.54(10)\,\mu_{\mathrm{B}}$, $M_y = 0.84(14)\,\mu_{\mathrm{B}}$, and $M_z = 2.12(10)\,\mu_{\mathrm{B}}$ yielding a total ordered moment of $M = 3.4(2)\,\mu_{\mathrm{B}}$. This model only describes the components ordered antiferromagnetically according to the commensurate propagation vector. We can deduce from the magnetization at 2 K [cf. Fig. 2(c)] that the field applied along $\vec{b}$ induces an additional ferromagnetic moment of about $M_{\mathrm{FM}} = 1.3\,\mu_{\mathrm{B}}$ further enhancing the total ordered moment. This ferromagnetic moment leads to an increase of intensity at the nuclear Bragg peak positions. The ratio between the components along $\vec{c}$ and $\vec{a}$ amounts to $M_z/M_x \approx 0.8$, which corresponds to an angle of 39.7° to the a axis. This value is significantly smaller than in the incommensurate zero-field phase.

Finally, Fig. 10(b) shows the model of the magnetic structure determined with the zero-field data directly after decreasing the field from 5 to 0 T at a constant temperature of 1.6 K. The propagation vector in the LF-C phase is the same as in the high-field phase, $\vec{k}_{\mathrm{com}} = (0.5,0.5,0.5)$. The system thus does not transform back to the low-field low-temperature LF-IC phase that is reached upon zero-field

TABLE V. Comparison of magnetic structures in $NaFe(WO_4)_2$ in magnetic fields applied parallel to $\vec{b}$. The orientation of the moments in the crystallographic unit cells are given and the corresponding propagation vectors are $\vec{k}_{\mathrm{com}} = (0.5,0.5,0.5)$ (C) and $\vec{k}_{\mathrm{inc}} = (0.485,0.5,0.48)$ (IC). The models were determined from experiments at D10 and 6T2 using FULLPROF [32]. We list the Fourier coefficients $\vec{M}$ for site 1 and the symmetry relation for site 2, with $a = e^{-2\pi i\cdot k_z\cdot r_z}$. The induced ferromagnetic magnetization, $M_{\mathrm{FM}}(B)$, is deduced from SQUID data.

$B\|\|b$ (T)	$M_{\mathrm{FM}}(B)$ (μ_B)	phase	site 1 $\vec{M}$ (μ_{B})	site 2	$\angle(\vec{e}_{ac},\vec{a})$ (°)	M_{tot} (μ_B)
0	0	LF-IC	$(3.3, -i\cdot 1.1, 3.6)$	$a\cdot(u,\bar{v},w)$	47.7	3.5
5	1.28	HF-C	(2.5, 0.8, 2.1)	$(\bar{u},\bar{v},\bar{w})$	39.7	3.6
3	0.75	HF-C	(3.0, 0.8, 3.0)	$(\bar{u},\bar{v},\bar{w})$	44.8	4.4
2	0.50	HF-C	(3.0, 0.5, 3.3)	$(\bar{u},\bar{v},\bar{w})$	48.1	4.5
1	0.25	LF-C	(2.7, 1.5, 3.3)	$(u,\bar{v},w)$	50.4	4.5
0	0	LF-C	(2.5, 2.1, 3.1)	$(u,\bar{v},w)$	50.7	4.5

cooling. This resembles observations in multiferroic $R\mathrm{MnO_3}$, which also exhibit a first-order phase transition from an incommensurate to a commensurate magnetic state upon enhancing the magnetic field and which also does not fall back to the initial magnetic structure after full release of the field [37,38]. In contrast to $R\mathrm{MnO_3}$, there is only one element carrying a magnetic moment in $\mathrm{NaFe(WO_4)_2}$, which documents that such hysteresis effects can just arise from pinning due to anharmonicity and single-ion anisotropy.

The same comparison of models was performed as described before and the best fit for the LF-C structure was achieved with canted moments in the crystallographic unit cell with components along all three axis: $M_x = 2.5(3)\ \mu_\mathrm{B}$, $M_y = 2.1(2)\ \mu_\mathrm{B}$, and $M_z = 3.1(4)\ \mu_\mathrm{B}$ yielding a total ordered moment of $M = 4.5(6)\ \mu_\mathrm{B}$, close to the expected value. The ratio between the components along $\vec{c}$ and $\vec{a}$ amounts to $M_z/M_x \approx 1.2$, which corresponds to an angle of 50.7° to the a axis. This value is similar to the one in the high-field phase. The transition from the HF-C to the LF-C phase is visible in a modulation of scattered intensity [cf. Fig. 9(b)] and as a spin-flop transition in the magnetization data [cf. Fig. 2(d)]. A comparison of the models in the incommensurate low-field phase (IC-LF), commensurate high-field phase (C-HF), and the commensurate low-field phase (C-LF) is given in Table V.

Common to both commensurate structures, LF-C and HF-C, is the up-up-down-down arrangement of spins along the zigzag chains parallel to $\vec{c}$. Such a structure can be considered as highly anharmonic as ferro- and antiferromagnetic neighbors alternate. The sizable magnetoelastic effect at the magnetic transition, which was observed in the thermal-expansion data, can be directly related to this anharmonic modulation. The AF1 ground state of isostructural $\mathrm{MnWO_4}$ also develops up-up-down-down chains of spins [19]. The transition towards this magnetic structure in $\mathrm{MnWO_4}$ is also accompanied with a drastic change in the thermal expansion, but its strength is reduced by an order of magnitude relative to $\mathrm{NaFe(WO_4)_2}$ [39].

VI. MAGNETOELASTIC COUPLING IN $\mathrm{NaFe(WO_4)_2}$

Two aspects of the above described magnetoelastic coupling are astonishing. First, the effects are rather large yielding a relative reduction of the b lattice parameter by up to $\frac{\Delta b}{b} \simeq -2.6 \times 10^{-4}$, and, second, there is no magnetoelastic anomaly at the onset of magnetic ordering in zero field, which results in the incommensurate phase. In most systems with strong magnetoelastic effects one may couple the strain, ϵ, with some power of the ordered moment defined as $m_{av} = \langle |m| \rangle$ [26–30,40], but in $\mathrm{NaFe(WO_4)_2}$ the intermediate incommensurate phase renders the analysis more complex. Apparently there is only a weak coupling to the incommensurate phase, while that to the commensurate order parameter is strong.

A deeper insight in the magnetoelastic coupling can be obtained from the Landau theory incorporating powers of the order parameter and strain terms to the expansion of the free energy [41]. For the commensurate ordering with doubling of the lattice along a and c directions, which corresponds to the up-up-down-down scheme in the chains, a linear quadratic coupling term in the free energy is allowed, because η_com^2 corresponds to the zone center. One may thus write the strain-dependent part of the free energy as [41]

$$F_\mathrm{strain} = a \cdot \epsilon \eta_\mathrm{com}^2 + C\epsilon^2, \tag{1}$$

where $a \cdot \epsilon \eta_\mathrm{com}^2$ describes the coupling between strain and the commensurate order parameter and $C\epsilon^2$ the purely elastic energy of the deformation. Minimizing the free energy with respect to ϵ, i.e., $\frac{\partial F}{\partial \epsilon} = 0$, yields the common proportionality between the strain and the square of the order parameter [41]:

$$\epsilon \propto \eta_\mathrm{com}^2. \tag{2}$$

In $\mathrm{NaFe(WO_4)_2}$, we do not observe a second-order phase transition to the commensurate phase, but the qualitative prediction of the Landau theory remains correct for small structural deformations also in case of first-order transitions. We may thus qualitatively understand the structural anomalies when entering the commensurate phase.

When extending this simple Landau theory one should first include the incommensurate character of the structural distortion, which requires taking into account two order parameter components (corresponding to the incommensurate wave vectors q and $-q$), which, however, can be transformed to an amplitude, A, and a phase, Φ. Only the amplitude couples to the strain, in the same way as described by Eq. (2) [41]. The competition between incommensurate and anharmonic or commensurate structural phases can be modeled by the umklapp terms yielding a contribution $VA^p \cos(p\Phi)$ to the free energy [41]. Here, the commensurate wave vector is $\frac{1}{p}\mathbf{G}$ with $\mathbf{G}$ a reciprocal lattice vector, and V is the energy constant. In our case this will yield a quadratic term which can be expected to be strong. There are purely structural systems displaying sequences of incommensurate and commensurate phases [42], and for example thermal-expansion measurements on $\mathrm{Rb_2ZnCl_4}$ found stronger anomalies at the incommensurate to commensurate transition [42] somewhat similarly to our observation. However, in $\mathrm{Rb_2ZnCl_4}$ there still is a sizable anomaly at the incommensurate transition, and the integrated length change in the incommensurate phase is even larger than that at the transition to commensurate order. The main shortcoming of the Landau theory to describe $\mathrm{NaFe(WO_4)_2}$ consists in its magnetic character and the fact that the transitions between the various phases appear when ordered moments are sizable and close to the saturation values. Therefore a microscopic magnetic model and its coupling to structural distortions are needed to describe the transition between the different phases in $\mathrm{NaFe(WO_4)_2}$. It is worth emphasizing that the sequence of magnetic transitions in $\mathrm{NaFe(WO_4)_2}$ resembles that in $R\mathrm{MnO_3}$. For decreasing ionic radius of the R ion in $R\mathrm{MnO_3}$ the magnetic structure changes from an incommensurate cycloid at $R = \mathrm{Tb}$ or Dy to an up-up-down-down structure at smaller R [1].

For the microscopic magnetic model, we restrict ourselves to the nearest-neighbor, J_N, and next-nearest-neighbor interactions, J_{NN}, along the chains in a simple Heisenberg Hamiltonian

$$H = \sum_{\langle i,j \rangle} J_{i,j} S_i \cdot S_j; \tag{3}$$

see Fig. 8(b). It is obvious that the commensurate structure satisfies an antiferromagnetic J_{NN}. However, the nearest-neighbor coupling J_N remains fully frustrated, so that there is no effective coupling between the upper and lower rows of the zigzag chain shown in Fig. 8(b). This resembles the J_1/J_2 frustrated square two-dimensional Heisenberg AFM model with nearest- and next-nearest-neighbor interaction which results in a frustration lifting distortion [43,44]. Adding intrachain terms does not lift this frustration in NaFe$(WO_4)_2$. One may also deduce from the simple commensurate structure that the structural symmetry must become triclinic. The up-up and down-down pairs in the zigzag chains point either along the bc or the $b\bar{c}$ diagonal, see Fig. 1(b), so that the twofold axis along b is broken. The dominating J_{NN} will enforce the commensurate up-up-down-down magnetic structure, but the persisting frustration of J_N is lifted by a triclinic distortion, which seems to be coupled with the larger and therefore visible effect in the b lattice parameter. This lifting of a degenerate state by a structural and ferroelastic distortion is rather common; it has been reported, e.g., for the J_1/J_2 frustrated square two-dimensional Heisenberg AFM model [44], for VOCl [29], $BaMn_2O_3$ [30], $BaCo_2V_2O_8$ [45], and the parent materials of FeAs-based superconductors [40]. Since the symmetry conditions are the same for the low-temperature commensurate phase of $MnWO_4$ the same analysis can be applied, and indeed magnetoelastic anomalies were also reported for this material but they are much smaller than in NaFe$(WO_4)_2$ [39]. The up-up-down-down magnetic structure should also result in some atomic displacements following either the parallel or antiparallel alignments. The determination of these displacements requires a dedicated structural analysis in the commensurate phase, which can only be reached by applying a magnetic field. Such a structural modulation would furthermore resemble the dimerization at the spin-Peierls transition in $CuGeO_3$, which also shows huge effects in the macroscopic strain parameters as well as soliton effects [46–49]. In contrast to the up-up-down-down case, there is no frustration left in the incommensurate magnetic structure, which is reflected by the fact that there is a single Fe orbit in this magnetic symmetry analysis; see Table II. There is thus no need for a structural distortion to lift magnetic frustration, which seems the reason for the absence of strong magnetoelastic coupling.

NaFe$(WO_4)_2$ also exhibits a magnetoelastic anomaly when the incommensurate structure becomes anharmonic, and the change in the b lattice parameter scales well with the intensity of the third-order satellite; see Fig. 5(e). The variation of the incommensurability seems to couple with the anharmonicity and therefore also scales with the length changes. The length change at the transition to an anharmonic incommensurate structure can be best understood when the incommensurate phase is described within a soliton-like model with antiphase domains and a varying order-parameter amplitude $\eta(x)$ that is either plus or minus η_{com}. The small anharmonic modulation thus implies regions with commensurate order. Note that the incommensurability, i.e., the deviation from the commensurate propagation vector in NaFe$(WO_4)_2$, is very small, so that the modulation length or the soliton distance amounts to about 50 lattice constants. Therefore the induced commensurate ordering results in qualitatively the same reduction of the b lattice parameter. From Fig. 5, one can see that the overall contraction $\frac{\Delta b}{b} \simeq -1.3 \times 10^{-4}$ between about 4 and 0.5 K is of similar magnitude to that of the field-induced contraction $\frac{\Delta b}{b} \simeq -1.5 \times 10^{-4}$ at the lower critical field $B_{c1}^{\text{up}} \simeq 3.8$ T and low temperature, whereas a significantly larger contraction $\frac{\Delta b}{b} \simeq -2.6 \times 10^{-4}$ takes place in a field of 7 T upon cooling. At high field, NaFe$(WO_4)_2$ directly transforms from the paramagnetic to the commensurate order, while this transition is split into two steps upon cooling and subsequent ramping up of the field. The sum of the length changes at the latter two transitions nicely agrees with that at cooling in high fields.

VII. CONCLUSIONS

The double tungstate NaFe$(WO_4)_2$ structurally resembles the well-studied spiral multiferroic $MnWO_4$ and its magnetic structure exhibits analogies with that in the RMnO$_3$ series where incommensurate cycloid and commensurate up-up-down-down phases compete. The magnetic phase diagram of NaFe$(WO_4)_2$ was investigated in detail. An analysis of the different magnetic structures by neutron diffraction together with the study of the complex temperature and magnetic field dependence of the propagation vector explains the magnetic phase diagram and the strong signature of magnetic phase transitions in various macroscopic measurements.

At zero magnetic field, the Fe^{3+} magnetic moments order directly in a spin spiral with an incommensurate propagation vector $\vec{k}_{\text{inc}} = (0.485,0.5,0.48)$ at 3.9 K. The spiral is elliptically distorted with the major axis of the spiral pointing along $\vec{e}_{ac}$ and the minor axis along $\vec{b}$. This phase can be described by a single one-dimensional irreducible representation. The incommensurability decreases with temperature and freezes in at a temperature of 2.0 K. Upon heating, the incommensurability shows a hysteresis behavior, which is coupled to an anharmonic distortion of the spiral. The hysteresis effects of the propagation vector and of the anharmonic distortion explain strong anomalies visible in thermal-expansion data, whereas the antiferromagnetic transition itself is almost invisible in thermal expansion.

The direct transition into the spiral state contrasts to other systems such as $MnWO_4$ and $TbMnO_3$, where the spiral phase follows a primarily sinusoidal modulated phase [19,50]. The spiral transition can be described by a single irreducible representation, which perfectly explains the absence of an electric polarization in this phase in NaFe$(WO_4)_2$. Spin spirals of opposite rotation sense are equally present in the system and cancel out the emergence of a macroscopic ferroelectric polarization as described by the inverse Dzyaloshinskii-Moriya coupling. In contrast, for $MnWO_4$ the spiral state is described by a combination of two representations, which allows for the unique chirality that induces a finite electric polarization.

In magnetic fields applied along $\vec{b}$, the magnetic structure becomes commensurate with a propagation vector $\vec{k}_{\text{com}} = (0.5,0.5,0.5)$. The collinear ordered magnetic moment possesses components within the monoclinic plane, as well as perpendicular to it. When the field is decreased while keeping the temperature constant, the magnetic order shows a spin-flop transition. The propagation vector remains commensurate but the magnetic moments are canted. This phase is similar to the commensurate ground state of $MnWO_4$ [19] but clearly differs from the low-temperature incommensurate phase that is reached in NaFe$(WO_4)_2$ upon zero-field cooling. The transition from incommensurate to commensurate magnetic order is accompanied by strong magnetoelastic anomalies, similar to those associated with the emergence of anharmonic components in the LF-IC phase. This similar magnetoelastic response can be explained by the character of the strongly anharmonic phase, which corresponds to commensurate parts separated by a regular arrangement of domain walls. Two aspects of the magnetoelastic coupling are remarkable: It is restrained to the commensurate, schematically up-up-down-down structure, and it is very strong yielding a relative length change of up to $\frac{\Delta b}{b} = 2.6 \times 10^{-4}$.

From the magnetic phase diagram we can assume that the magnetic ground state of $\mathrm{NaFe(WO_4)_2}$ is the commensurate low-field phase with an almost fully ordered moment while the LF-IC phase is metastable and exhibits an ordered moment significantly below that expected for $S = 5/2$. Upon cooling, the system first orders in the incommensurate structure with a sizable anharmonic distortion developing below ~3 K. But even on further cooling the system does not transform to the LF-C phase. Applying magnetic fields along $\vec{b}$ at low temperature induces the transition into the commensurate state, which persists even after full reduction of the field.

Overall the phase diagram of $\mathrm{NaFe(WO_4)_2}$ is governed by the interplay of anharmonic distortions and structures with the single-ion anisotropy. For $\mathrm{Fe^{3+}}$, the single-ion anisotropy is expected to be small but significant contributions were also observed in $AB\mathrm{FeO_4}$ (with A = La, Pr and B = Sr, Ca) [51,52]. In $\mathrm{NaFe(WO_4)_2}$, the impact of the $\mathrm{Fe^{3+}}$ single-ion anisotropy seems enhanced by the weakness of the magnetic exchange. Pinning of anharmonic modulations should furthermore be relevant for the understanding of the magnetoelectric memory and switching behavior of closely related multiferroics.

ACKNOWLEDGMENTS

This work was supported by the Deutsche Forschungsgemeinschaft through the Bonn Cologne Graduate School and through CRC 1238 Projects No. A02, No. B01, and No. B04.

[1] S. W. Cheong and M. Mostovoy, Nat. Mater. **6**, 13 (2007); S. Dong and J.-M. Liu, Mod. Phys. Lett. B **26**, 1230004 (2012).

[2] T. Kimura, S. Ishihara, H. Shintani, T. Arima, K. Takahashi, K. Ishizaka, and Y. Tokura, Nature (London) **426**, 55 (2003).

[3] H. Katsura, N. Nagaosa, and A. V. Balatsky, Phys. Rev. Lett. **95**, 057205 (2005).

[4] M. Mostovoy, Phys. Rev. Lett. **96**, 067601 (2006).

[5] I. A. Sergienko and E. Dagotto, Phys. Rev. B **73**, 094434 (2006).

[6] I. A. Sergienko, C. Sen, and E. Dagotto, Phys. Rev. Lett. **97**, 227204 (2006).

[7] S. Ishiwata, Y. Kaneko, Y. Tokunaga, Y. Taguchi, T.-H. Arima, and Y. Tokura, Phys. Rev. B **81**, 100411(R) (2010).

[8] R. Valdés Aguilar, M. Mostovoy, A. B. Sushkov, C. L. Zhang, Y. J. Choi, S.-W. Cheong, and H. D. Drew, Phys. Rev. Lett. **102**, 047203 (2009).

[9] T. Finger, K. Binder, Y. Sidis, A. Maljuk, D. N. Argyriou, and M. Braden, Phys. Rev. B **90**, 224418 (2014).

[10] O. Heyer, N. Hollmann, I. Klassen, S. Jodlauk, L. Bohatý, P. Becker, J. Mydosh, T. Lorenz, and D. Khomskii, J. Phys.: Condens. Matter **18**, L471 (2006).

[11] A. H. Arkenbout, T. T. M. Palstra, T. Siegrist, and T. Kimura, Phys. Rev. B **74**, 184431 (2006).

[12] K. Taniguchi, N. Abe, T. Takenobu, Y. Iwasa, and T. Arima, Phys. Rev. Lett. **97**, 097203 (2006).

[13] S. Jodlauk, Ph.D. thesis, Universität zu Köln, 2010.

[14] H. Cid-Dresdner and C. Escobar, Z. Kristallogr. **127**, 61 (1968).

[15] H. Weitzel, Z. Kristallogr. **144**, 238 (1976).

[16] L. Nyam-Ochir, H. Ehrenberg, A. Buchsteiner, A. Senyshyn, H. Fuess, and D. Sangaa, J. Magn. Magn. Mater. **320**, 3251 (2008).

[17] P. Klevtsov and R. Klevtsova, J. Solid State Chem. **2**, 278 (1970).

[18] E. F. Bertaut, Acta Crystallogr. **A24**, 217 (1968).

[19] G. Lautenschläger, H. Weitzel, T. Vogt, R. Hock, A. Böhm, M. Bonnet, and H. Fuess, Phys. Rev. B **48**, 6087 (1993).

[20] J. M. Perez-Mato, J. L. Ribeiro, V. Petricek, and M. I. Aroyo, J. Phys.: Condens. Matter **24**, 163201 (2012).

[21] I. Urcelay-Olabarria, J. M. Perez-Mato, J. L. Ribeiro, J. L. García-Muñoz, E. Ressouche, V. Skumryev, and A. A. Mukhin, Phys. Rev. B **87**, 014419 (2013).

[22] T. Finger, D. Senff, K. Schmalzl, W. Schmidt, L. P. Regnault, P. Becker, L. Bohatý, and M. Braden, J. Phys.: Conf. Ser. **211**, 012001 (2010).

[23] K. Taniguchi, N. Abe, S. Ohtani, and T. Arima, Phys. Rev. Lett. **102**, 147201 (2009).

[24] T. Finger, D. Senff, K. Schmalzl, W. Schmidt, L. P. Regnault, P. Becker, L. Bohatý, and M. Braden, Phys. Rev. B **81**, 054430 (2010).

[25] J. Rossat-Mignod, J. Phys. Colloques **40**, C5-95 (1979).

[26] C. Vecchini, M. Poienar, F. Damay, O. Adamopoulos, A. Daoud-Aladine, A. Lappas, J. M. Perez-Mato, L. C. Chapon, and C. Martin, Phys. Rev. B **82**, 094404 (2010).

[27] A. C. Komarek, H. Roth, M. Cwik, W.-D. Stein, J. Baier, M. Kriener, F. Bourée, T. Lorenz, and M. Braden, Phys. Rev. B **75**, 224402 (2007).

[28] T. Kimura, Y. Tomioka, A. Asamitsu, and Y. Tokura, Phys. Rev. Lett. **81**, 5920 (1998).

[29] A. C. Komarek, T. Taetz, M. T. Fernandez-Diaz, D. M. Trots, A. Möller, and M. Braden, Phys. Rev. B **79**, 104425 (2009).

[30] M. Valldor, O. Heyer, A. C. Komarek, A. Senyshyn, M. Braden, and T. Lorenz, Phys. Rev. B **83**, 024418 (2011).

[31] K. G. Dergachev, Low Temp. Phys. **31**, 402 (2005).

[32] J. Rodriguez-Carvajal, Phys. B: Condens. Matter **192**, 55 (1993).

[33] D. Khomskii, *Transition Metal Compounds* (Cambridge University Press, Cambridge, 2014).

[34] M. Ackermann, Ph.D. thesis, Universität zu Köln, 2014.

[35] I. V. Solovyev, Phys. Rev. B **87**, 144403 (2013).

[36] N. Qureshi, E. Ressouche, A. A. Mukhin, V. Y. Ivanov, S. N. Barilo, S. V. Shiryaev, and V. Skumryev, Phys. Rev. B **88**, 174412 (2013).

[37] D. Senff, P. Link, N. Aliouane, D. N. Argyriou, and M. Braden, Phys. Rev. B **77**, 174419 (2008).

[38] J. Baier, D. Meier, K. Berggold, J. Hemberger, A. Balbashov, J. A. Mydosh, and T. Lorenz, Phys. Rev. B **73**, 100402(R) (2006).

[39] R. P. Chaudhury, F. Yen, C. R. dela Cruz, B. Lorenz, Y. Q. Wang, Y. Y. Sun, and C. W. Chu, Physica B **403**, 1428 (2008).

[40] C. de la Cruz, Q. Huang, J. W. Lynn, J. Li, W. Ratcliff II, J. L. Zaretsky, H. A. Mook, G. F. Chen, J. L. Luo, N. L. Wang *et al.*, Nature (London) **453**, 899 (2008).

[41] R. A. Cowley, Adv. Phys. **29**, 1 (1980); A. D. Bruce and R. A. Cowley, *Structural Phase Transitions* (Taylor and Francis Ltd., London, 1981).

[42] R. Blinc, P. Prelovŝek, V. Rutar, J. Seliger, and S. Žumer, in *Incommensurate Phases in Dielectrics, 1, Fundamentals*, edited by R. Blinc and A. P. Levanyuk (North-Holland Physics Publishing, Amsterdam, 1986), p. 143.

[43] P. Chandra, P. Coleman, and A. I. Larkin, Phys. Rev. Lett. **64**, 88 (1990).

[44] R. Melzi, P. Carretta, A. Lascialfari, M. Mambrini, M. Troyer, P. Millet, and F. Mila, Phys. Rev. Lett. **85**, 1318 (2000).

[45] S. K. Niesen, G. Kolland, M. Seher, O. Breunig, M. Valldor, M. Braden, B. Grenier, and T. Lorenz, Phys. Rev. B **87**, 224413 (2013).

[46] H. Winkelmann, E. Gamper, B. Büchner, M. Braden, A. Revcolevschi, and G. Dhalenne, Phys. Rev. B **51**, 12884(R) (1995).

[47] R. Rückamp, J. Baier, M. Kriener, M. W. Haverkort, T. Lorenz, G. S. Uhrig, L. Jongen, A. Möller, G. Meyer, and M. Grüninger, Phys. Rev. Lett. **95**, 097203 (2005).

[48] T. Lorenz, B. Büchner, P. H. M. van Loosdrecht, F. Schönfeld, G. Chouteau, A. Revcolevschi, and G. Dhalenne, Phys. Rev. Lett. **81**, 148 (1998).

[49] B. Büchner, T. Lorenz, R. Walter, H. Kierspel, A. Revcolevschi, and G. Dhalenne, Phys. Rev. B **59**, 6886 (1999).

[50] M. Kenzelmann, A. B. Harris, S. Jonas, C. Broholm, J. Schefer, S. B. Kim, C. L. Zhang, S.-W. Cheong, O. P. Vajk, and J. W. Lynn, Phys. Rev. Lett. **95**, 087206 (2005).

[51] N. Qureshi, H. Ulbrich, Y. Sidis, A. Cousson, and M. Braden, Phys. Rev. B **87**, 054433 (2013).

[52] N. Qureshi, M. Valldor, L. Weber, A. Senyshyn, Y. Sidis, and M. Braden, Phys. Rev. B **91**, 224402 (2015).